Journal of Glaciology

Article

Cite this article: Sun P, Yang W, Tuhkuri J (2024). Mechanical properties of pressure-frozen ice under triaxial compressive stress. *Journal of Glaciology* 1–9. https://doi.org/10.1017/jog.2024.59

Received: 13 November 2023
Revised: 22 May 2024
Accepted: 29 May 2024

Keywords:
cracking; ice; pressure-frozen ice; strength of ice; triaxial compressive test

Corresponding author:
Weihao Yang;
Email: cumt_whyang@163.com

cambridge.org/jog

Mechanical properties of pressure-frozen ice under triaxial compressive stress

Peixin Sun[1], Weihao Yang[1,2] and Jukka Tuhkuri[3]

[1]State Key Laboratory for Geomechanics and Deep Underground Engineering, China University of Mining and Technology, Xuzhou, China; [2]School of Mechanics and Civil Engineering, China University of Mining and Technology, Xuzhou, China and [3]Department of Mechanical Engineering, Aalto University, Espoo, Finland

Abstract

Artificial ground freezing is an effective method for underground constructions in deep alluvium. To study the compressive strength of frozen soil under high ground pressure and high hydraulic pressure, it is necessary to understand the mechanical behaviour of ice that is formed under triaxial compressive stress. A low-temperature triaxial test system was developed and used to study both formation and deformation of columnar ice under hydrostatic pressure. Cylindrical ice specimens 125 mm in height and 61.8 mm in diameter were prepared and tested under constant strain rates. At a strain rate of $5 \times 10^{-5}\ s^{-1}$, the peak axial stress showed a linear increase as the confining pressure increased from 2 to 30 MPa, while the peak deviatoric stress exhibited a slight decrease. At a confining pressure of 30 MPa, the peak deviatoric stress showed a logarithmic increase with the strain rate increasing from 5×10^{-6} to $5 \times 10^{-4}\ s^{-1}$, and the failure strain nearly doubled. A power law relationship between the time to failure and the strain rate was also observed. In this study, each test consistently demonstrated a ductile failure mode, with a noticeable reduction in cracking as the confining pressure increased. Due to the effect of the high confining pressure, crack propagation was suppressed, and an apparent recrystallization after peak stress was observed.

1. Introduction

1.1. Artificial ground freezing

Coal resources are abundant in China, with a total amount of 5.97 trillion tons. However, 53% of these resources are buried at depths exceeding 1000 m, and in the eastern and north-eastern regions, many valuable deposits are covered by deep alluvium (Cui, 1998). A vertical shaft, with a diameter of 5–15 m and a depth of several hundred metres, is typically constructed to serve as the primary passage for facilities and personnel entering and exiting the mine tunnel. Artificial ground freezing (AGF) is an effective method for constructing vertical shafts and other deep underground projects in water-bearing surface soil layers (Bai and others, 2020). The fundamental principle in ground freezing is to convert pore water into ice. Initially, a freezing station is constructed to continuously generate low-temperature brine. Subsequently, a series of holes is drilled radially around the proposed vertical shaft, penetrating through soil or rock layers. Refrigerant circulation pipes (referred to as 'freezing pipes') are then inserted into these holes, with each freezing pipe serving as the central point for freeze-up. As the freezing process advances, adjacent frozen soil (or rock) gradually intersects to form a closed circular structure, known as a 'frozen wall'. This frozen wall not only withstands ground pressure but also prevents the inflow of groundwater, ensuring safe and efficient excavation. However, the mechanical properties of the ice-bearing soil/rock mass within the frozen wall are complex and not well understood, leading to inaccurate estimations of the design thickness of the frozen wall. On one hand, if the strength of the frozen soil body is underestimated, it will result in unnecessary construction costs. On the other hand, if the strength of the frozen soil body is overestimated, considering the creep behaviour of the frozen soil, it may undergo large deformations or even sudden instability and failure during its service period, leading to irreversible substantial losses.

Much research has been devoted to the mechanical properties of frozen soil and rock in the context of deep earth and cold region engineering construction (Lai and others, 2013; Shan and others, 2015; Gao and others, 2020; Kuang and others, 2022). As a binding agent, ice provides the cohesive force within frozen soil or rock. It is also critical to note the significant influence that ice lenses (or segregated ice) exert on the mechanical properties of permafrost (Shan and others, 2017; Wang and others, 2018). Figure 1 illustrates the application of AGF in shaft sinking and the formation of ice lenses in the freezing process.

1.2. Ice mechanics study

Following investigations in the 1950s and 1960s on ice deformation (Rigsby, 1951, 1957, 1960; Glen and Perutz, 1954; Glen, 1955; Langway, 1958; Glen and Jones, 1966), a multitude of studies on the triaxial mechanical properties of sea ice and fresh water ice have been conducted. Some employed constant strain rate tests, while others utilized constant stress tests (creep

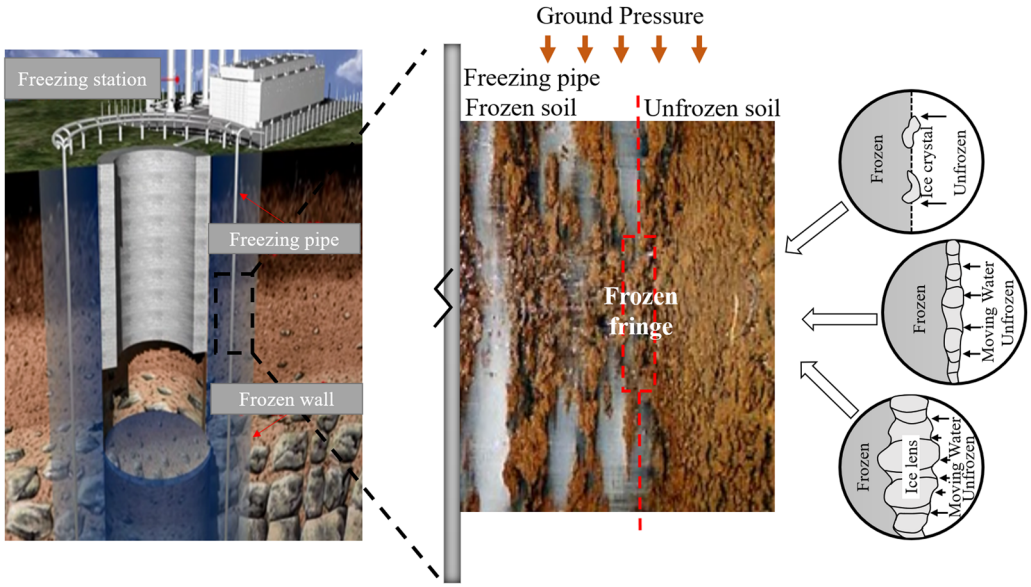

Figure 1. Diagram of the artificial ground freezing (AGF) method for shaft sinking and the formation of ice lenses.

tests). Deformation of ice in a laboratory setting was best described by Glen's flow law, which takes strain rate, deviatoric stress, activation energy and temperature (Glen, 1955) into consideration. The impact of confining pressure and strain rate on strength was non-monotonic; furthermore, these two factors exhibited mutual influence (Goughnour and Andersland, 1968). At low temperatures and high strain rates, the fracture behaviour of ice showed a pressure dependence similar to that observed in brittle rocks, where strength increased with confining pressure (Nawwar and others, 1983; Cox and Richter-Menge, 1988; Richter-Menge, 1991; Gagnon and Gammon, 1995). However, at higher temperatures and pressures, strength was independent of pressures or decreased slightly with further increase in confinement (Jones, 1982; Durham and others, 1983; Kirby and others, 1985; Nadreau and Michel, 1986; Murrell and others, 1991; Rist and Murrell, 1994; Rist and others, 1994). Under a given confining pressure and temperature, a transition occurred from ductile to brittle behaviour upon raising strain rate (Schulson, 1990). Meanwhile, fine-grained ice was more prone to behaving in a ductile manner and had higher strength compared to columnar ice or coarse-grained ice (Cole, 1985; Mizuno, 1998). This could be due to its larger grain boundary area, resulting in a stronger capacity for energy absorption.

The brittle failure process has been well studied and can be described by the fault triggering mechanism incorporating both frictional sliding and splay cracking (Schulson and others, 1989, 1991; Gratz and Schulson, 1997; Schulson and Gratz, 1999; Schulson and Renshaw, 2022). The ductile failure process was mainly caused by micro-fracturing and recrystallization. Under high hydrostatic pressure combined with shear, a reduction of grain size was observed, indicative a deformation mechanism of very different nature than those operating at lower levels of pressure. (Meglis and others, 1999; Melanson and others, 1999; Barrette and Jordaan, 2001, 2003; Jordaan and others, 2005).

However, although there have been numerous studies on the mechanical response of ice under multiaxial compressive loading, there is still limited research available on ice formed in soils at high pressures (at depth), here referred to as pressure-frozen soil. First and foremost, it is necessary to develop a technique for freezing water specimens into ice under high confining pressure. Following this, triaxial tests of pressure-frozen ice should be conducted at different temperature, confining pressure, strain rate, etc. The ultimate goal of this research is to determine which findings from previous studies on sea ice or fresh water ice align with those on pressure-frozen ice, and which can be applied to deep-ground engineering and explore whether pressure-frozen ice possesses any unique properties.

In this paper, a novel method for preparing ice specimens under pressure of 30 MPa was firstly introduced. Then, constant strain rate (from 5×10^{-6} to 5×10^{-4} s^{-1}) triaxial tests were conducted at a temperature of −10°C, and the effect of confining pressure (from 2 to 30 MPa) and strain rate on mechanical properties of pressure-frozen ice were analysed. Finally, by combining observations of specimens after loading with thin sections taken at different loading stages, the failure mode of ice was initially discussed.

2. Apparatus and specimen preparation

2.1. Apparatus

A servo-controlled low-temperature triaxial testing system to grow and test ice under pressure was developed (Fig. 2). The system consisted of a triaxial cell inside which ice specimens are studied; a load frame housing the cell and providing axial load; oil, an oil pump, and a pressure volume controller to provide confining pressure; and a cooling system. The system is capable of imposing an axial load up to 400 kN and a confining pressure up to 64 MPa, with accuracies of 0.01 and 0.1%, respectively. The axial force was measured with a load cell. A 60 mm-thick insulation jacket was wrapped around the triaxial cell to prevent excessive inward heat flow from the surroundings. Two thermocouple rods were created to monitor the temperature of specimen and oil.

2.2. Fabrication of water specimen

The specimen space was constructed using two end caps and one heat-shrinkable tubing. One of the end caps was composed of inner and outer caps linked together through a threaded fastening method. The other end cap, located on the central axis, featured a water injection hole equipped with a closure bolt (Fig. 3a). An assembly cylinder was created, comprising an internal positioning column and four external split tubes. The column consisted of two sections: a long section matching the outer cap's inner diameter and a shorter section matching the water injection

https://doi.org/10.1017/jog.2024.59 Published online by Cambridge University Press

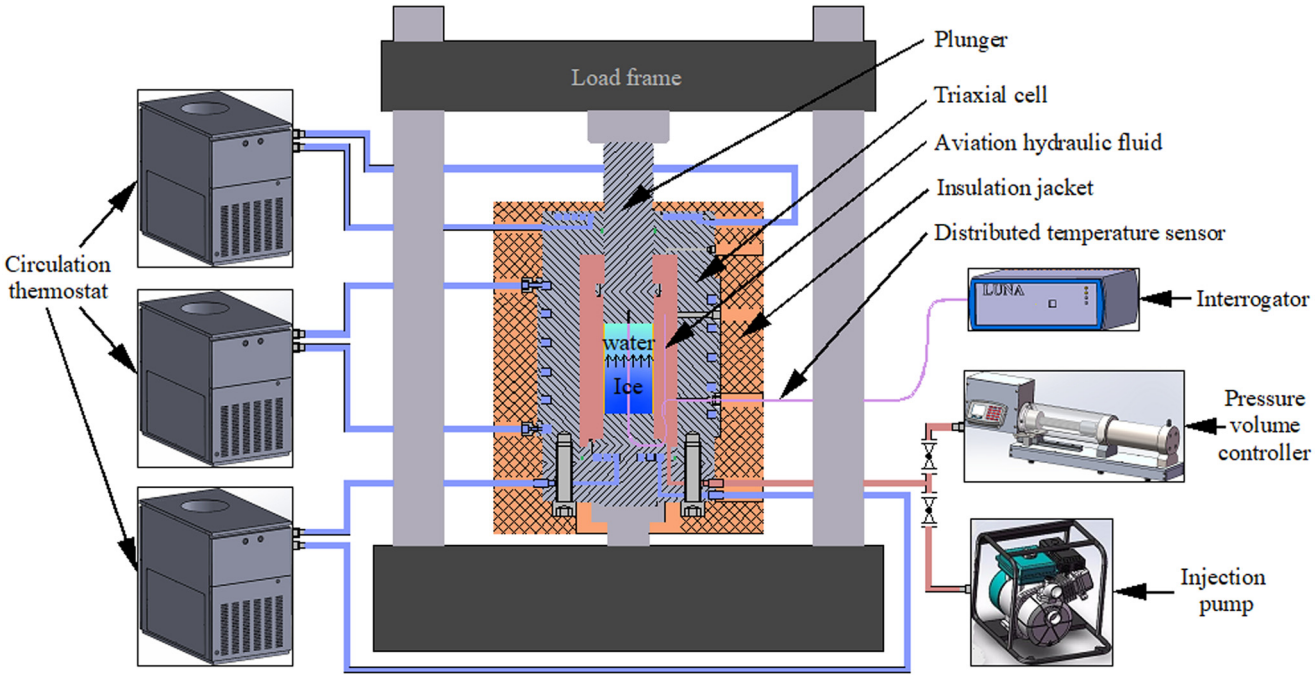

Figure 2. KTL-401 servo-controlled low-temperature triaxial testing system.

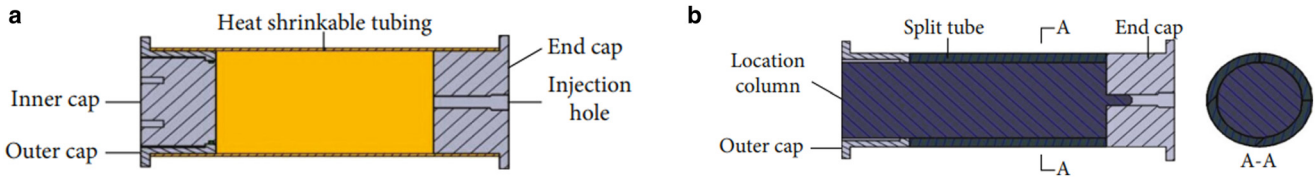

Figure 3. The components of (a) end caps and (b) assembly cylinder.

hole's inner diameter. Split tubes were partitioned equally along the circumference, each sharing the external size of the water specimen and the inner diameter of the outer cap (Fig. 3b).

During the fabrication process, the outer cap and end cap were placed separately at the ends of the positioning column. Split tubes were then assembled around the outside to form the cylinder assembly. A specific type of low-temperature-resistant adhesive with a slow curing speed was applied to the cap surfaces. Heat shrink tubing was applied over the entire structure, heated to tightly encase the caps and split tubes. Once the adhesive has fully cured, the positioning column and split tubes are removed through the outer cap. Finally, securing the inner cap to the outer cap completed the water specimen package. After filling the package with degassed distilled water through the water injection hole and tightening the closure bolt, the final cylindrical water specimen was obtained.

A mounting device (Fig. 4), comprising a fixed platform and a lifting platform, was designed to ensure the water specimen is not deformed due to the gravity exerted by the upper end cap and plunger during the insertion process. The lifting platform was equipped with a hanger and two hanger rods. The upper and lower end caps are securely attached to the plunger and baseplate, respectively. The plunger was threaded connected to hanger rods and suspended within the pressure vessel, with the baseplate resting on the lifting platform. Subsequently, the lifting platform elevates both the plunger and the baseplate in perfect synchrony, ensuring the insertion of the water specimen without any deformation. Following this step, the baseplate and pressure vessel were securely fastened together using eight equally spaced bolts to form the triaxial cell, which was then transported to the load frame. The final step involves connecting all the necessary conduits, completing the assembly of the test system.

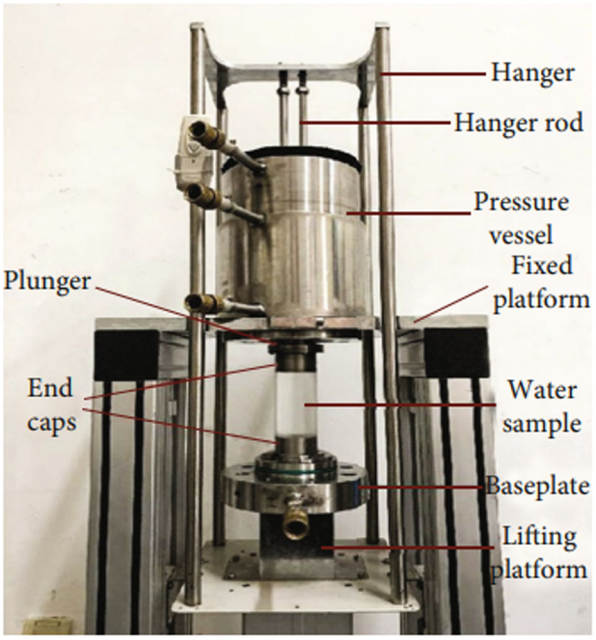

Figure 4. Mounting device.

https://doi.org/10.1017/jog.2024.59 Published online by Cambridge University Press

2.3. Preparation of pressure-frozen ice specimen

The oil was injected to the triaxial cell by the oil pump. After the injection process was completed, the water specimen was pressurized to 30 MPa at a speed of 0.2 MPa s^{-1} by the pressure volume controller.

The cooling system consisted of circulation thermostats, and freezing channels located inside the upper, lateral and lower parts of the triaxial cell (Fig. 2). The freezing channels were connected to thermostats to circulate the ethyl alcohol at 2°C (in the upper channel) and −30°C (in the lower channel) in order to freeze the water specimen from bottom to top.

In the context of this study, both freezing and loading were conducted continuously under pressure. To ensure that the water specimen maintains a standard cylindrical shape after freezing, it is crucial to control the volume of oil during the freezing process. For example, if no measures are taken, the hydraulic oil will lose volume because of cold-induced contraction and the water specimen will expand along both axial and radial directions when freeze-up occurs, rather than forming a standard cylinder, and the specimen diameter will exceed that of the loading rod. Thus, in our work, oil was continuously replenished during the freezing process in order to compensate for the volume loss and force the specimen to expand only along the axial direction, by constraining the radial expansion. With the appropriate replenishment rate, the pressure was maintained at 30 MPa throughout the freezing process. After the freezing process was completed, the lateral channel was used to circulate the ethyl alcohol at −15°C for 5 h, ensuring a uniform specimen temperature of −10°C.

Before commencing the formal experiments, several preliminary trials were conducted to investigate the temperature evolution during the freezing process and the uniformity of the specimen's temperature. Five thermocouples were evenly attached to a glass fibre rod and fixed along the central axis inside the specimen, while an additional four thermocouples were fixed outside the specimen (as shown in Fig. 5). They were used to measure the temperature of the specimen and hydraulic oil. Figure 6 displays the temporal variations of hydraulic oil temperature, specimen temperature and the volume of oil replenishment over time. Based on the temperature data of the oil, the replenishment amount at each moment can be calculated, approximated with a piecewise linear function for operational convenience (black dashed line in Fig. 6). Temperature data of the specimen indicated that, after 5 h of circulating the ethyl alcohol at −15°C (in the lateral channel), the specimen's temperature stabilized at (−10 ± 0.3)°C. Among them, points A and E showed temperatures around −9.7 to −9.8°C, while points B, C and D showed slightly lower temperatures, approximately −10.3°C.

Two preliminary experiments were conducted to determine if the specimen dimensions meet the requirements for triaxial testing. The average diameters of upper, medium and lower parts of specimens were 61.71, 61.73 and 61.92 mm, respectively, while the average height was 125.32 mm, meeting the standard size of 61.8 mm in diameter and 125 mm in height (Fig. 7a). Thin sections showed that the specimen was bubble-free, and the columnar ice had a grain size of 5.1 ± 0.6 mm (Figs 7b, c). The density remained stable, ranging from 0.915 to 0.916 g cm^{-3}.

3. Tests and results

3.1. Stress and strain measures

Axial stress σ_1 is defined by

$$\sigma_1 = \frac{F}{A}, \tag{1}$$

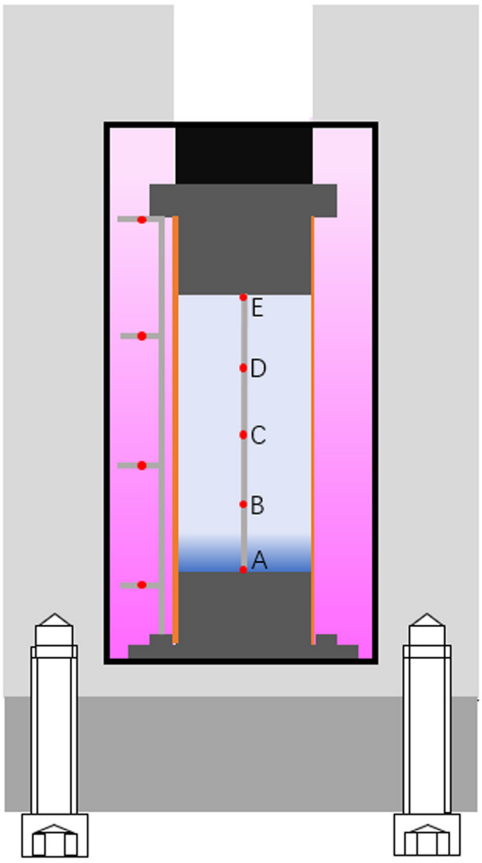

Figure 5. Layout of temperature measurement points.

where F is the axial force, acting between the loading rod and the specimen, directly measured by a load cell. A is the initial circular cross-sectional area, which is equal to 2998.1 mm^2.

Radial stress σ_3 is equal to the confining pressure. Deviatoric stress is defined as the difference between the axial stress and the radial stress, which is represented by σ_1–σ_3.

Axial true strain ϵ_1 is defined by

$$\varepsilon_1 = \int \frac{\mathrm{d}\delta_s}{h}, \tag{2}$$

where δ_s is the deformation of the specimen and h is the instantaneous length of the specimen.

The deformation of a test specimen is not directly measured but is calculated by

$$\begin{aligned}\delta_s &= \delta - \delta_f, \quad \delta_f \\ &= (4.64 \times 10^{-2}) + (7.2 \times 10^{-3})F - (1 \times 10^{-5})F^2 \\ &\quad + (1 \times 10^{-8})F^3,\end{aligned} \tag{3}$$

where δ is the displacement of the loading device and is measured during a test. δ_f is the deformation of the load frame, and was obtained through a calibration using a 304 stainless steel specimen with the same dimensions as the ice specimen and a compression stiffness of 194 GPa. Based on this, a formula for calculating the deformation of load frame δ_f from the axial force F is obtained through polynomial fitting, where δ, δ_s and δ_f are measured in millimetres (mm), F is measured in kilonewtons (kN), and the units of the coefficients are determined by the power of F.

https://doi.org/10.1017/jog.2024.59 Published online by Cambridge University Press

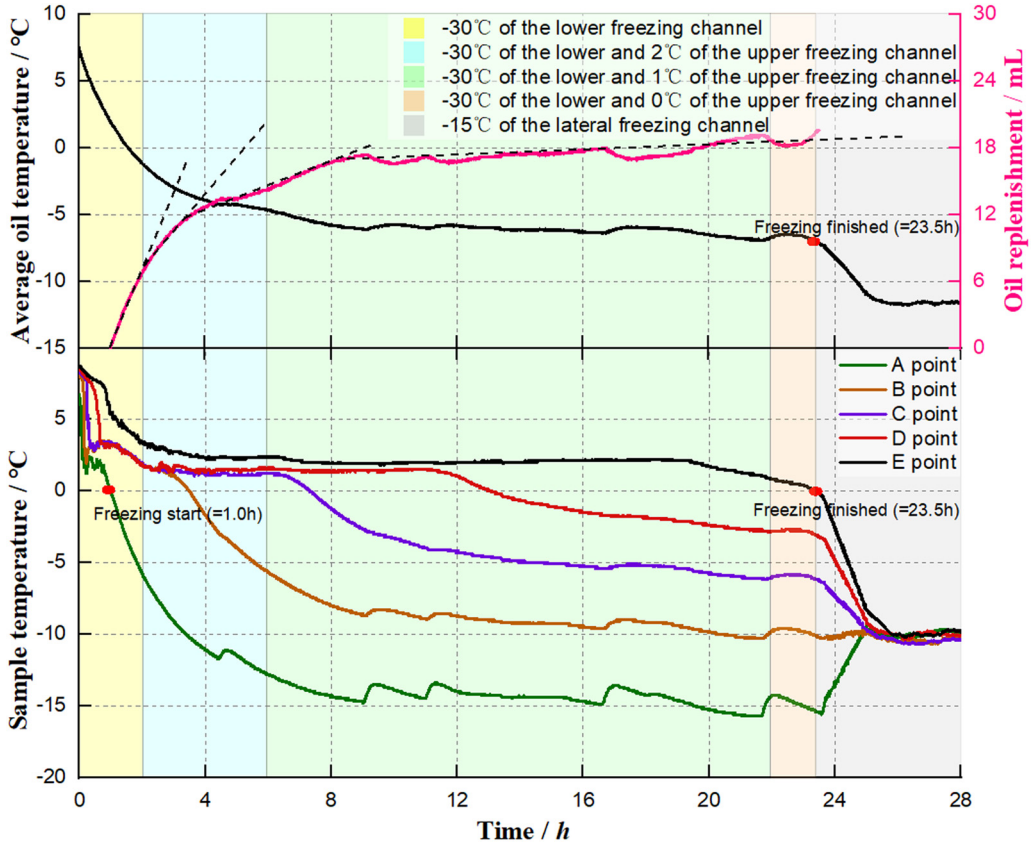

Figure 6. Temperature of oil and specimen and the volume of oil replenishment over time.

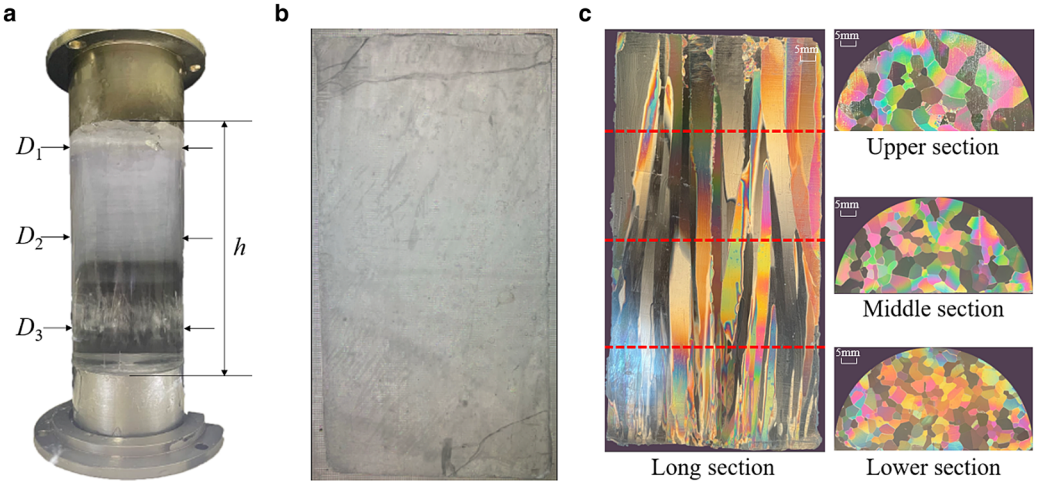

Figure 7. Pictures of (a) ice specimen, (b) thin section under natural light and (c) thin sections viewed through crossed polaroids.

3.2. Experimental scheme

Figure 8 shows the schematic diagram of loading and unloading. Once the freezing was completed, the confinement was immediately adjusted from the freezing pressure to the confining (testing) pressure. To prevent damage, a maximum rate of 0.5 MPa min^{-1} was used. Here, the freezing pressure σ_f is 30 MPa, representing the pressure applied during the freezing process. σ_c means the confining pressure during triaxial tests, ranging from 2 to 30 MPa. Axial force was applied in a constant strain rate, ranging from 5×10^{-6} to 5×10^{-4} s^{-1}, and the loading was stopped when the axial strain reached 5%. After tests, the deviatoric stress was firstly unloaded at a rate of 0.05 mm min^{-1}, and then, the axial stress and radial stress were synchronously unloaded to zero at a rate of 0.33 MPa min^{-1}. Finally, the oil was drained, and the specimen was removed from the cell.

3.3. Test results

Test results are summarized in Table 1, and axial stress–axial strain curves are shown in Figure 9. The peak point on the stress–strain curve corresponds to the peak axial stress σ_{1p}, where the difference of peak axial stress and confining pressure is the peak strength (or peak deviatoric stress). The axial strain at the highest point is regarded as the failure strain ϵ_{1p}. The deviatoric stress at 5% axial strain corresponds to the residual strength. The stress–strain curves consistently demonstrated a pattern of

https://doi.org/10.1017/jog.2024.59 Published online by Cambridge University Press

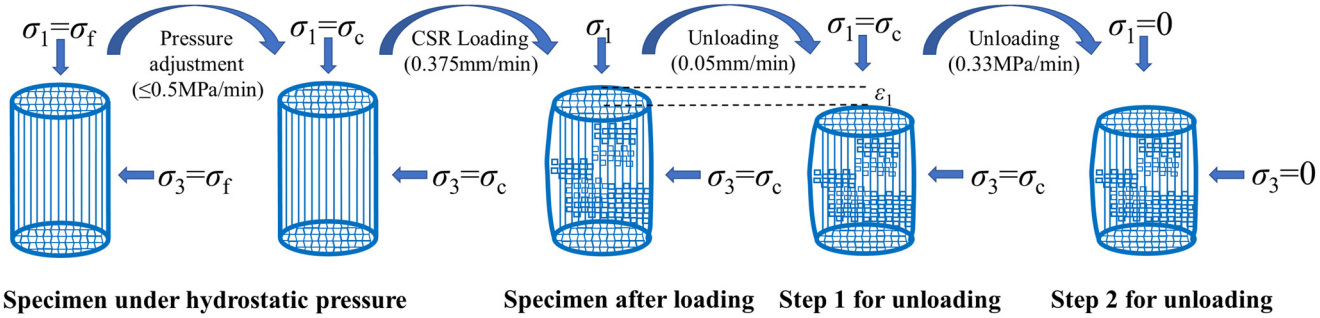

Figure 8. Schematic diagram of loading and unloading.

Table 1. Summary of test results

Test group No.	Freezing pressure σ_f MPa	Confining pressure σ_c MPa	Strain rate $\dot{\varepsilon}$ s^{-1}	Peak axial stress σ_{1p} MPa	Peak strength σ_{1p}-σ_c MPa	Failure strain ϵ_{1p} %	Residual stress σ_{1r}-σ_c MPa
A1	30	2	5×10^{-5}	15.23	13.23	0.76	3.08
A2	30	5	5×10^{-5}	16.12	11.12	0.90	4.54
A3	30	10	5×10^{-5}	22.55	12.55	0.68	4.68
A4	30	20	5×10^{-5}	29.41	9.41	0.78	3.78
A5	30	30	5×10^{-5}	41.70	11.70	0.64	4.46
A6	30	30	10^{-4}	43.60	13.60	0.75	5.05
A7	30	30	2×10^{-4}	45.22	15.22	0.93	4.67
A8	30	30	5×10^{-4}	53.87	23.87	1.38	16.11
A9	30	30	5×10^{-6}	36.15	6.15	0.64	2.72

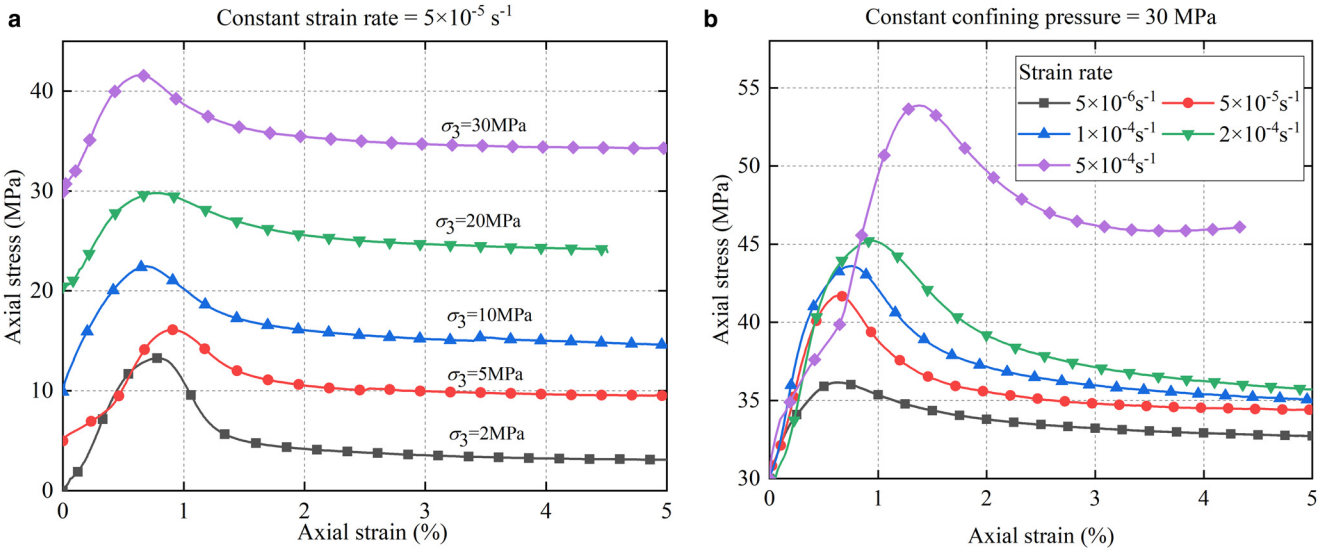

Figure 9. Axial stress–axial strain curves at (a) different confining pressure and at (b) different strain rates.

strain-softening. In the initial stage, stress and strain exhibited a linear relationship. After reaching the peak, the ice entered the softening stage where the stress decreased, exhibiting a noticeable post-peak inflection point. Ultimately, the specimen reached the plastic flow stage, where the stress remained nearly constant.

4. Discussion

4.1. Effect of confining pressure

At a strain rate of 5×10^{-5} s^{-1} (Fig. 10), the peak axial stress showed a linear increase with confining pressure. At a confining pressure of 2 MPa, the strength measured 15.2 MPa, and it increased to 41.7 MPa when subjected to a confining pressure of 30 MPa. The axial stress and confining pressure exhibited a linear relationship with a slope of 0.90, less than unity, which means the peak deviatoric stress slightly decreases as the confining pressure increased from 2 to 30 MPa. Previous experiments on polycrystalline ice have showed that at a temperature of (−11.8 ± 0.9)°C and a strain rate of 5.5×10^{-5} s^{-1}, the strength of polycrystalline ice (fine-grained ice) under confining pressures of 10, 20 and 30 MPa is reported to be 6–7 MPa. However, the strength of columnar-grained ice in this study is around 10 MPa (Jones, 1982). This could be attributed to a higher proportion of grain boundary area in polycrystalline ice, making it more prone to softening. Besides, the failure strain in all tests was <1%, with the range of 0.64–0.90%, and the average of 0.76%. The average residual strength was 4.11 MPa, with a minimum of 3.08 MPa occurring at a confining pressure of 2 MPa, and a maximum of 4.68 MPa occurring at a confining pressure of 10 MPa.

https://doi.org/10.1017/jog.2024.59 Published online by Cambridge University Press

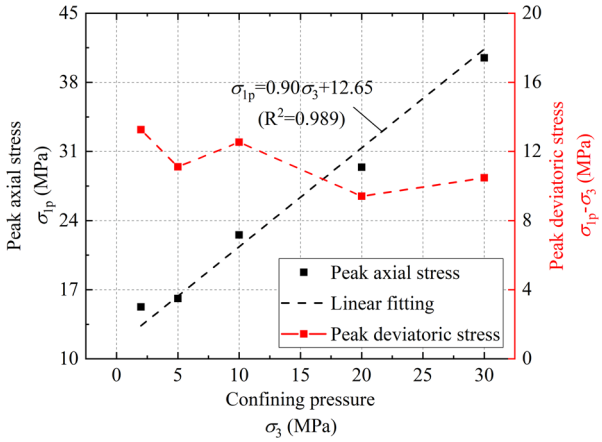

Figure 10. Dependence of peak axial stress and peak deviatoric stress on confining pressure at a strain rate of 5×10^{-5} s^{-1}.

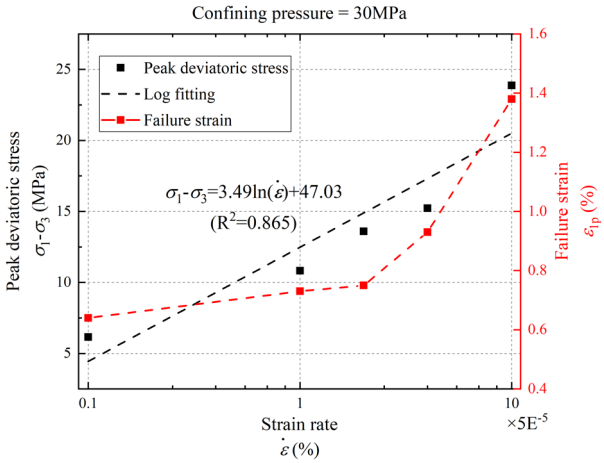

Figure 11. Dependence of peak deviatoric stress and failure strain on strain rate at a confining pressure of 30 MPa.

Currently, with reference to the construction of shafts using artificial freezing as an example, the depth of soil and water-rich rock penetration has surpassed 750 and 950 m, respectively (Dai and Wang, 2019). Theoretical estimates suggest that the water pressure within the soil layer nears 8–10 MPa, alongside an approximate vertical ground stress of 20 MPa. Considering the localized pressure increase resulting from freezing expansion during freezing operations, the underground water pressure involved will exceed 10 MPa. In the rock layers, water pressure spans from 15 to 25 MPa, while vertical stress may exceed 65 MPa. The findings of this study reveal that the peak axial stress in ice under a confining pressure of 30 MPa is 2.7 times higher than that under a confining pressure of 2 MPa. This implies that, for deep underground construction projects involving high-pressure frozen soil, rock or ice excavation, the utilization of more effective drilling and blasting methods or more robust equipment is warranted to overcome the increasing strength associated with depth or overburden pressure. In addition, the confinement during ice growth, the freezing pressure, could have affected the ice strength. The freezing pressure may decrease the porosity and air volume of the ice, thus increasing the strength, but it is also possible that any air in the pores is under pressure causing local tensile stresses within the ice. Further, as the freezing pressure was not removed before the strength tests, any stresses formed in the ice during the freezing process were not able to undergo any relaxation before measuring the strength.

4.2. Effect of strain rate

At a confining pressure of 30 MPa, the peak deviatoric stress showed a linear increase with the logarithm of strain rate. When the strain rate increased from 5×10^{-6} to 5×10^{-4} s^{-1}, the strength of ice increased from 6.15 to 23.87 MPa, and the failure strain nearly doubled from 0.64 to 1.38% (Fig. 11). This serves as a reminder that when using machinery such as the tunnel boring machine for excavating through ice or frozen soil layers, it is crucial to carefully control the excavation speed, as excessively high rates can lead to accelerated wear and tear on components.

In addition, the time from the start of loading to reaching peak strength is defined as the time to failure t_f. It was found that the failure time and the strain rate have a power function relationship (Fig. 12), that fits the following equation:

$$t_f = 3.48\dot{\varepsilon}^{-0.85}. \quad (4)$$

The power exponent is close to that of previous uniaxial tests which were carried out for columnar ice with grain size of 4–5 mm at −10°C, where it was found to be −0.82 (Sinha, 1982). Within the ductile range, a lower strain rate provides more time for the evolution of internal damage of the ice specimen, ultimately may leading to a lower strength.

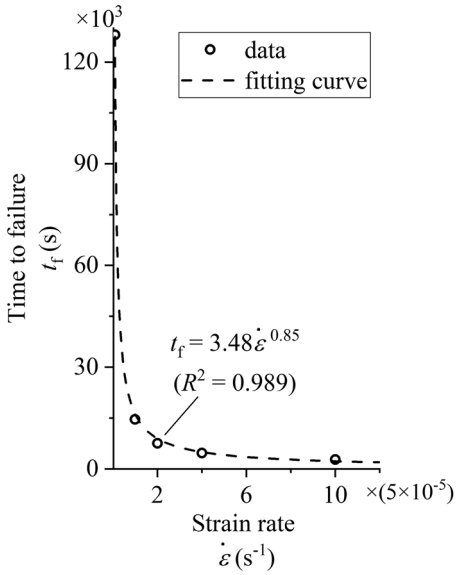

Figure 12. Dependence of the time to failure on strain rate.

4.3. Failure mode

The stress–strain curves of all tests in this paper exhibited ductile behaviour, with stress showing a gradual softening after reaching the peak point, rather than a sudden decrease. However, there were still some differences in cracking. At a strain rate of 5×10^{-5} s^{-1}, with confining pressures of 2 MPa and 10 MPa, numerous fishbone-like and wing-shaped cracks were observed, and a higher confining pressure resulted in reduced cracking. When the confining pressure was 30 MPa, even if the strain was loaded to 5%, the ice was still transparent and clear, without visible cracks. With the increase of strain rate, although a small number of fine microcracks appeared, it was still almost clear (Fig. 13). This suggests that confining pressure plays a role in limiting crack nucleation and growth, which is consistent with previous observations of polycrystalline ice (Rist and Murrell, 1994). In the earlier creep tests of multiyear sea ice at confining pressure

https://doi.org/10.1017/jog.2024.59 Published online by Cambridge University Press

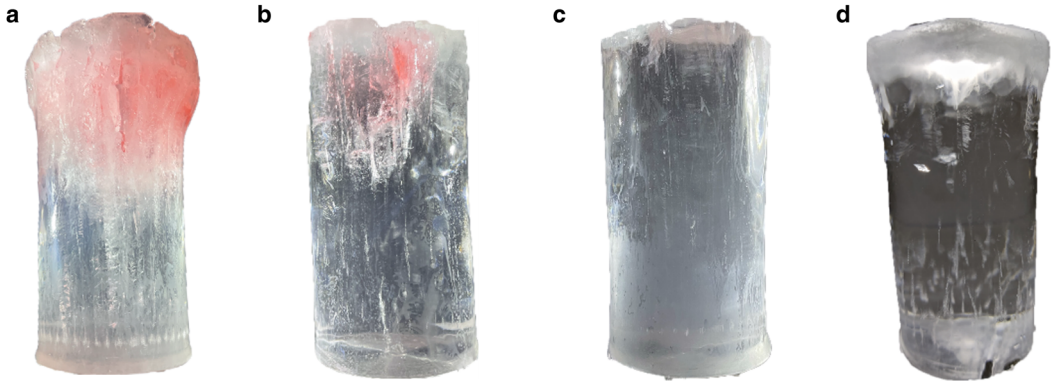

Figure 13. Crack distribution when loaded to 5% strain.

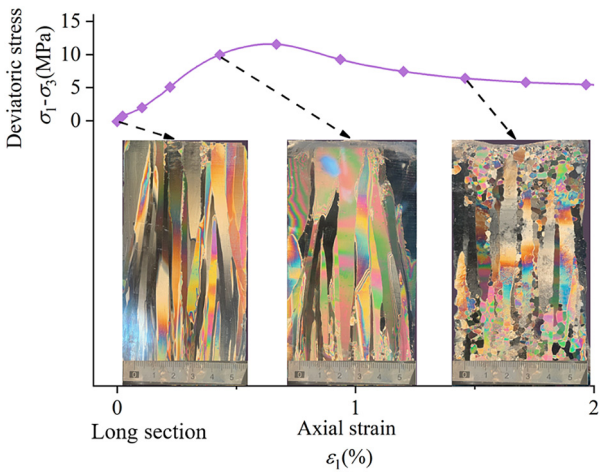

Figure 14. Thin sections of different loading stage at a confining pressure of 30 MPa and a strain rate of $5 \times 10^{-5}\,s^{-1}$.

of 30 MPa, strain rate of $10^{-2}\,s^{-1}$, and temperature of −10°C, it was also observed that cracking was completely inhibited (Sammonds and others, 1998).

Thin sections of specimens of axial strain $\epsilon_1 = 0$, 0.5, 1.5% at a confining pressure of 30 MPa and a strain rate of $5 \times 10^{-5}\,s^{-1}$ were made (Fig. 14). It was found that the columnar grains essentially maintained their initial appearance both before loading and when loaded to a strain of 0.5%, and the recrystallization was observed when the strain reached 1.5%. This reflects that under high confining pressure, the strain-softening behaviour of ice may be primarily driven by dynamic recrystallization (DRX). In the future, more experiments should be taken to study if there are clear relationships between DRX and confining pressure or strain rate.

5. Conclusions

Using a self-developed low-temperature triaxial test system, cylindric columnar ice specimens were made for constant strain rate triaxial tests. The main conclusions can be summarized as follows:

(1) A method for preparing pressure-frozen ice was described. By freezing the water specimen from bottom to top and replenishing the oil during freezing process, cylindric columnar ice specimens can be obtained, with the size of 125 mm in height and 61.8 mm in diameter, and its density is close to pure fresh water ice. Both freezing and testing were conducted continuously under pressure.

(2) Constant strain rate triaxial tests of 30 MPa pressure-frozen ice at −10°C in the range of confining pressure of 2–30 MPa and strain rate of 5×10^{-6} to $5 \times 10^{-4}\,s^{-1}$ were conducted. At a constant strain rate of $5 \times 10^{-5}\,s^{-1}$, the peak axial stress showed a linear increase with confining pressure, while the peak deviatoric stress exhibited a slight decrease.

(3) At a confining pressure of 30 MPa, the peak deviatoric stress showed a linear increase with the logarithm of strain rate, and the failure strain has nearly doubled, when the strain rate increased from 5×10^{-6} to $5 \times 10^{-4}\,s^{-1}$. It was also found that the time to failure and the strain rate have a power law relationship.

(4) Each set of tests exhibited a ductile failure mode, although with some variations. The failure mode of ice includes macro-scale crack propagation and micro-scale recrystallization. Cracking was suppressed by high confining pressure. Recrystallization occurred after the specimen reached peak strength, and its correlation with confining pressure and loading rate warrants further investigation.

(5) The focal point of deep-earth research lies in recreating (or simulating) high-pressure environments in the laboratory. The freezing and testing method proposed in this paper, along with its characteristic of maintaining controlled stress states throughout the entire process, facilitates the conduction of triaxial tests under different stress paths. For example, confining pressure reduction tests can reflect lateral unloading conditions in wells (or boreholes), while axial pressure reduction tests can reflect bottom unloading conditions.

Acknowledgements. This work was funded by the Assistance Program for Future Outstanding Talents of China University of Mining and Technology (grant No. 2022WLKXJ120), the Postgraduate Research & Practice Innovation Program of Jiangsu Province (grant No. KYCX22_2584) and the Shanghai Science and Technology Committee Rising-Star Cultivating Program (grant No. 22YF1418300).

References

Bai Y and 5 others (2020) Study on the mechanical properties and damage constitutive model of frozen weakly cemented red sandstone. *Cold Regions Science and Technology* **171**, 102980. doi: 10.1016/j.coldregions.2019.102980

Barrette PD and Jordaan IJ (2001) Creep of ice and microstructural changes under confining pressure. In Murakami S and Ohno N (eds), *IUTAM Symposium on Creep in Structures. Solid Mechanics and its Applications*, Vol **86**. Dordrecht: Springer, pp. 479–488, doi: 10.1007/978-94-015-9628-2_46

Barrette PD and Jordaan IJ (2003) Pressure-temperature effects on the compressive behavior of laboratory-grown and iceberg ice. *Cold Regions Science and Technology* **36**(1–3), 25–36. doi: 10.1016/s0165-232x(02)00077-0

Cole DM (1985) Grain size and the compressive strength of ice. *Journal of Energy Resources Technology* **107**(3), 369–374. doi: 10.1115/1.3231203

Cox GFN and Richter-Menge JA (1988) Confined compressive strength of multi-year pressure ridge sea ice samples. *Journal of Offshore Mechanics and Arctic Engineering* **110**, 295–301. doi: 10.1115/1.3257065

Cui GX (1998) Mechanics of frozen soil for deep alluvium – a new field of frozen soil mechanics. *Journal of Glaciology and Geocryology* **20**(2), 97–100. doi: 10.7522/j.issn.1000-0240.1998.0022

Dai HD and Wang QC (2019) Experimental study on mechanical properties of frozen soil in deep soil of Wanfu coal mine. *Journal of Mining Science and Technology* **4**(2), 120–126. doi: 10.19606/j.cnki.jmst.2019.02.004

Durham WB, Heard HC and Kirby SH (1983) Experimental deformation of polycrystalline H_2O ice at high pressure and low temperature: preliminary results. *Journal of Geophysical Research* **88**(S01), B377–B392. doi: 10.1029/jb088is01p0b377

Gagnon RE and Gammon PH (1995) Triaxial experiments on iceberg and glacier ice. *Journal of Glaciology* **41**(139), 528–540. doi: 10.3189/s0022143000034869

Gao F, Cao SP, Zhou KP, Lin Y and Zhu LY (2020) Damage characteristics and energy-dissipation mechanism of frozen-thawed sandstone subjected to loading. *Cold Regions Science and Technology* **169**, 102920. doi: 10.1016/j.coldregions.2019.102920

Glen JW (1955) The creep of polycrystalline ice. *Proceedings of the Royal Society A* **228**(1175), 519–538. doi: 10.1098/rspa.1955.0066

Glen JW and Jones SJ (1966) The deformation of ice single crystals at low temperatures. *Physics of Snow and Ice: Proceedings* **1**(1), 267–275. doi: 10.3189/002214354793702434

Glen JW and Perutz MF (1954) The growth and deformation of ice crystals. *Journal of Glaciology* **2**(16), 397–403. doi: 10.3189/002214354793702434

Goughnour RR and Andersland OB (1968) Mechanical properties of a sand-ice system. *Journal of the Soil Mechanics and Foundations Division* **94**(4), 923–950. doi: 10.1061/jsfeaq.0001179

Gratz ET and Schulson EM (1997) Brittle failure of columnar saline ice under triaxial compression. *Journal of Geophysical Research* **102**(B3), 5091–5107. doi: 10.1029/96jb03738

Jones SJ (1982) The confined compressive strength of polycrystalline ice. *Journal of Glaciology* **28**(98), 171–178. doi: 10.1017/s0022143000011874

Jordaan IJ, Barrette PD, Duval P and Meyssonnier J (2005) Mechanisms of ice softening under high pressure and shear. Proceedings of the International Conference on Port and Ocean Engineering under Arctic Conditions, 26–30 June 2005, Potsdam, New York, Vol 1, 249–259.

Kirby SH, Durham WB and Heard HC (1985) Rheologies of H20 ices Ih, II, and III at high pressures: a progress report. In Klinger J, Benest D, Dollfus A and Smoluchowski R (eds), *Ices in the Solar System*. NATO ASI Series, Vol **156**. Dordrecht: Springer, pp. 89–107, doi: 10.1007/978-94-009-5418-2_7

Kuang LF, Mo PQ, Wang KJ and Chen B (2022) An elastic-plastic solution for the optimal thickness of a frozen soil wall considering an interaction with the surrounding rock. *PLoS ONE* **17**(4), e0267014. doi: 10.1371/journal.pone.0267014

Lai YM, Xu XT, Dong YH and Li SY (2013) Present situation and prospect of mechanical research on frozen soils in China. *Cold Regions Science and Technology* **87**, 6–18. doi: 10.1016/j.coldregions.2012.12.001

Langway CC (1958) Ice fabrics and the universal stage. US Army Snow Ice and Permafrost Research Establishment.

Meglis IL, Melanson PM and Jordaan IJ (1999) Microstructural change in ice: II. Creep behavior under triaxial stress conditions. *Journal of Glaciology* **45**, 438–448. doi: 10.3189/s0022143000001295

Melanson PM, Meglis IL, Jordaan IJ and Stone BM (1999) Microstructural change in ice: I. Constant-deformation-rate tests under triaxial stress conditions. *Journal of Glaciology* **45**, 417–422. doi: 10.1017/s0022143000001271

Mizuno Y (1998) Effect of hydrostatic confining pressure on the failure mode and compressive strength of polycrystalline ice. *Journal of Physical Chemistry B* **102**, 376–381. doi: 10.1021/jp963163b

Murrell SAF, Sammonds PR and Rist MA (1991) Strength and failure modes of pure ice and multi-year sea ice under triaxial loading. In Jones S, Tillotson J, McKenna RF and Jordaan IJ (eds), *Ice-Structure Interaction. International Union of Theoretical and Applied Mechanics*. Berlin, Heidelberg: Springer, pp. 339–361, doi: 10.1007/978-3-642-84100-2_17

Nadreau JP and Michel B (1986) Secondary creep in confined ice samples. Proceedings of the 8th IAHR International Symposium on Ice, 18–22 August, Iowa City, Iowa, Vol. 1, 307–318.

Nawwar AM, Nadreau JP and Wang YS (1983) Triaxial compressive strength of saline ice. Proceedings of the International Conference on Port and Ocean Engineering under Arctic Conditions, 5–9 April 1983, Espoo, Helsinki, Vol 3, 193–201.

Richter-Menge JA (1991) Confined compressive strength of horizontal first-year sea ice samples. *Journal of Offshore Mechanics and Arctic Engineering* **113**, 344–351. doi: 10.1115/1.2919940

Rigsby GP (1951) Crystal fabric studies on Emmons Glacier Mount Rainier, Washington. *Journal of Glaciology* **59**(6), 590–598. doi: 10.1086/625914

Rigsby GP (1957) Effect of hydrostatic pressure on velocity of shear deformation of single ice crystals. *Journal of Glaciology* **3**(24), 271–278. doi: 10.1017/S0022143000023911

Rigsby GP (1960) Crystal orientation in glacier and in experimentally deformed ice. *Journal of Glaciology* **3**(27), 589–606. doi: 10.1017/s0022143000023716

Rist MA and Murrell SAF (1994) Ice triaxial deformation and fracture. *Journal of Glaciology* **40**(135), 305–318. doi: 10.1017/s0022143000007395

Rist MA, Jones SJ and Slade TD (1994) Microcracking and shear fracture in ice. *Annals of Glaciology* **19**, 131–137. doi: 10.3189/1994aog19-1-131-137

Sammonds PR, Murrell SAF and Rist MA (1998) Fracture of multiyear sea ice. *Journal of Geophysical Research* **103**(C10), 21795–21815. doi: 10.1029/98jc01260

Schulson EM (1990) The brittle compressive fracture of ice. *Acta Metallurgica et Materialia* **38**(10), 1963–1976. doi: 10.1016/0956-7151(90)90308-4

Schulson EM and Gratz ET (1999) The brittle compressive failure of orthotropic ice under triaxial loading. *Acta Materialia* **47**, 745–755. doi: 10.1016/s1359-6454(98)00410-8

Schulson EM and Renshaw CE (2022) Fracture, friction, and permeability of ice. *Annual Review of Earth and Planetary Sciences* **50**, 323–343. doi: 10.1146/annurev-earth-032320-085507

Schulson EM, Gies MC, Lasonde GJ and Nixon WA (1989) The effect of the specimen-platen interface on internal cracking and brittle fracture of ice under compression: high-speed photography. *Journal of Glaciology* **35**, 378–382. doi: 10.1017/s0022143000009308

Schulson EM, Jones DE and Kuehn GA (1991) The effect of confinement on the brittle compressive fracture of ice. *Annals of Glaciology* **15**, 216–221. doi: 10.1017/s0260305500009769

Shan RL, Bai Y, Song LW and Song YW (2015) Experimental study of blasting vibration and damage characteristics on frozen shaft wall. *Chinese Journal of Rock Mechanics and Engineering* **34**(Supp. 2), 3732–3741. doi: 10.13722/j.cnki.jrme.2015.0603

Shan RL, Bai Y, Huang PC, Song YW and Guo X (2017) Experimental research on failure criteria of freshwater ice under triaxial compressive stress. *Chinese Journal of Theoretical and Applied Mechanics* **49**(2), 467–477. doi: 10.6052/0459-1879-16-364

Sinha NK (1982) Constant strain- and stress-rate compressive strength of columnar-grained ice. *Journal of Materials Science* **17**(3), 785–802. doi: 10.1007/bf00540376

Wang DY, Wang YT, Ma W, Lei LL and Wen Z (2018) Study on the freezing-induced soil moisture redistribution under the applied high pressure. *Cold Regions Science and Technology* **145**, 135–141. doi: 10.1016/j.coldregions.2017.10.012

https://doi.org/10.1017/jog.2024.59 Published online by Cambridge University Press